Imaging the displacement field within epitaxial nanostructures by coherent diffraction: a feasibility study

A. Diaz, Virginie Chamard, C. Mocuta, Rogerio Magalhães-Paniago, J. Stangl, D. Carbone, T.H. Metzger, G. Bauer

Imaging the displacement field within epitaxial nanostructures by coherent diffraction: a feasibility study

2010 New J. Phys. 12 035006

(http://iopscience.iop.org/1367-2630/12/3/035006)

New Journal of Physics
The open-access journal for physics

Imaging the displacement field within epitaxial nanostructures by coherent diffraction: a feasibility study

Ana Diaz[1,2,5,6], **Virginie Chamard**[3], **Cristian Mocuta**[4], **Rogerio Magalhães-Paniago**[1], **Julian Stangl**[2], **Dina Carbone**[1], **Till H Metzger**[1] **and Günther Bauer**[2]

[1] European Synchrotron radiation Facility, 6 rue Jules Horowitz, BP 220, 38043 Grenoble, France
[2] Institute of Semiconductor and State Solid Physics, Johannes Kepler Universität, Altenbergerstrasse 69, 4040 Linz, Austria
[3] Aix-Marseille Université and CNRS, IM2NP, FST av. Escadrille Normandie Niemen, 13397 Marseille Cedex, France
[4] Synchrotron Soleil, L'Orme des Merisiers, St. Aubin, BP 48, 91192 Gif-Sur-Yvette, France
E-mail: ana.diaz@psi.ch

New Journal of Physics **12** (2010) 035006 (20pp)
Received 30 September 2009
Published 31 March 2010
Online at http://www.njp.org/
doi:10.1088/1367-2630/12/3/035006

Abstract. We investigate the feasibility of applying coherent diffraction imaging to highly strained epitaxial nanocrystals using finite-element simulations of SiGe islands as input in standard phase retrieval algorithms. We discuss the specific problems arising from both epitaxial and highly strained systems and we propose different methods to overcome these difficulties. Finally, we describe a coherent microdiffraction experimental setup using extremely focused x-ray beams to perform experiments on individual nanostructures.

[5] Author to whom any correspondence should be addressed.
[6] Present address: Paul Scherrer Institute, 5232 Villigen PSI, Switzerland.

Contents

1. Introduction

Apart from the small size of nanostructures, the presence of strain can change the mechanical, electronic, optical and magnetic properties of materials. In the case of semiconductor nanostructures, for example, the strain may shift the wavelength of the light emitted by quantum dots [1] or increase the mobility of the charge carriers in CMOS devices [2]. The strain may be induced during the growth on the substrates, by surrounding matrices or more generally by interfaces, as in the case of intrinsic strain in core–shell nanostructures. In the literature we find many examples of nanostructures whose physical properties differ from their bulk counterparts [3]–[5]. The determination of atomic displacements inside epitaxial nanostructures is thus an important task and remains a challenge for x-ray diffraction.

The growth of nearly perfect epitaxial nanostructures, as demanded by technological applications, relies on matching crystal lattices between different materials. Any small mismatch results in atomic displacements in the nanostructure, with a related three-dimensional (3D) strain field [6, 7]. The quantification of such displacements is a big challenge as it requires methods capable of high spatial resolution in 3D and high strain sensitivity. X-ray scattering techniques are non-destructive, provide high resolution and element sensitivity, allow for *in-situ* and in-operation capabilities and thus make this approach preferable, under certain circumstances, to direct and invasive imaging techniques such as transmission electron microscopy (TEM) [8].

Strain in nanostructures has been extensively studied with x-ray diffraction [9, 10]: the main outcome is that the knowledge of lattice parameter and composition are essential prerequisites to determine the strain distribution. State-of-the-art analysis of x-ray diffraction data relies heavily on model assumptions, as for example the smooth variation of the lattice parameter inside the islands, which are typically refined by the use of fitting routines [11, 12]. Calculations using the finite-element method (FEM) have proven to be successful as long as the investigated systems are simple enough in order to assume an appropriate model [10, 13]. However, this is a difficult task for cases in which complex variations of chemical composition are present [14]. For these cases, a model-independent analysis technique is highly desirable. Furthermore, the usual FEM approach is based on linear continuum elasticity theory and does not include effects such as surface stress, for instance.

Coherent diffraction imaging (CDI) has recently emerged as a technique with great potential for the 3D determination of atomic displacement fields inside nanocrystals [15]. This lens-less imaging method became possible with the advent of highly brilliant third-generation synchrotron sources. It relies on the use of a coherent x-ray beam, whose wavefront has a well-defined phase relation that is preserved through the scattering process. Therefore, the complex-valued wavefield holds the information on the exact position of the single scatterers. When the scattered intensity is oversampled, i.e. sampled at a frequency larger than twice the Nyquist frequency ($\Delta Q < 2\pi/L$, with L a characteristic sample dimension [16]), the intensity pattern can be inverted by means of iterative phase retrieval algorithms [17]. The first demonstration of CDI was reported by Miao *et al* in 1999 [18] for a 2D non-crystalline test object, followed rapidly by the 3D demonstration [19]. Another important step was done by Robinson *et al* with the demonstration of nanocrystal imaging in 2D [20] and in 3D [21] from intensity patterns measured in Bragg geometry. More recently, the same group has presented the 3D reconstruction of the displacement field within a free-standing (i.e. non-epitaxial) Pb nanocrystal [22].

While CDI is encountering rapid development, with recent results in the imaging of complex non-crystalline materials [23] and biological samples [24], the case of strain field imaging remains more difficult to address and has been achieved only for selected nanostructures with a high atomic number, because it requires a particularly precise control of the experimental conditions. Indeed, the direct space retrieved phase, which relates to the strain field, can be affected by any local beam curvature, and/or the experimental resolution function (beam divergence, point spread detection, etc). This is especially critical when one attempts to address strain fields within weakly strained crystals [25, 26]. Fortunately, for larger strain fields the influence of the experimental conditions can be neglected. However, in these cases the convergence of the algorithm is often becoming a problem and one has to seek for additional direct space constraints, specific to the studied system, in order to reach the convergence [27].

The aim of our work is to use CDI for the 3D imaging of displacement fields within individual epitaxial nanostructures with a resolution of few tens of nanometers. This task turns out to be extremely challenging due to a number of experimental and fundamental difficulties intrinsic to epitaxial nanostructures. A first important issue is associated with the presence of the substrate on which the nanostructure is grown because it represents a non-finite extension of the nanostructure's real space. For the application of phase retrieval algorithms, the substrate rules out the use of the so-called 'finite support', which is a fundamental requisite for their convergence. Furthermore, the retrieval of large strain fields introduces complications in the convergence of phase retrieval algorithms. In this paper, we present a numerical study of the determination of strain in an epitaxial nanostructure by CDI. To this aim, we use SiGe nanocrystals epitaxially deposited on a Si substrate as a model system. Simulated diffraction profiles are determined on the basis of FEM calculations and iterative phase retrieval algorithms are applied in order to retrieve the displacement field within the nanostructures directly from the simulated diffraction patterns. The next step of our work will be to apply our proposed approaches to a set of experimental data. Despite the good quality of the data collected, our first attempts of phase retrieval have not been successful so far. On the basis of our simulations, we discuss which are the conditions the data have to satisfy for the convergence of the algorithms.

The paper is organized as follows: a detailed explanation of the model samples and the FEM simulations is given in section 2. In section 3, we discuss the difficulties related to the use of iterative algorithms on our particular epitaxial system. Different approaches to overcome these difficulties are presented in sections 4 and 5. The first approach consists of the realization

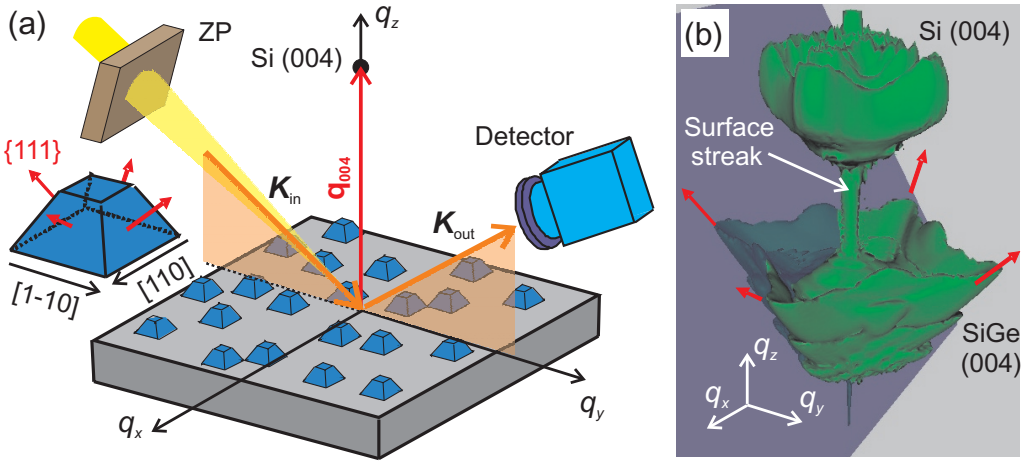

Figure 1. (a) Sketch of a micro-diffraction setup for the characterization of individual SiGe islands. The crystallographic orientation of the islands is shown with respect to the scattering geometry. Experimental details are explained in section 6. (b) Calculation of the 3D intensity distribution from an individual island around the Si (004) Bragg reflection. An iso-intensity surface is shown. The dark plane represents the intersection of the detector in the 3D reciprocal space at the Bragg condition corresponding to the SiGe (004) Bragg peak.

of a finite object by the finite illumination provided by a focusing device. In the second approach, an approximation that neglects the contribution of the substrate signal to the diffraction pattern is introduced. Finally, in section 6, we describe an experimental setup suited to perform coherent micro-diffraction experiments at third-generation synchrotron sources. We discuss here the existing gap between state-of-the-art experimental data and the requirements identified by our simulations.

2. Finite-element and x-ray diffraction calculations

The model system investigated here are SiGe islands grown by liquid phase epitaxy (LPE) with the method described in detail in [28]. The islands have the shape of a truncated square pyramid with a (001) top facet and {111} side facets, as shown in the sketch of figure 1(a). A common feature of LPE-grown islands is a distinct step in the Ge concentration at about 1/3 of their height, being lower in the bottom part and higher in the top part [29]. SiGe islands may also be grown by other techniques such as molecular beam epitaxy or chemical vapor deposition, which result in different, often multi-faceted island shapes, and pronounced gradients of the Ge content. In many cases, inhomogeneous island ensembles form, creating a demand for investigation of single islands.

In analyzing x-ray diffraction patterns from island ensembles as well as single islands, modeling approaches have been very successful in the past [10, 13]. Therefore, we use the structure of LPE-grown SiGe islands on Si(001) substrates as determined in [13] as the basis of our investigation. We consider a truncated pyramid with a base size of 140 nm, a height of 70 nm, and a Ge content of 20 and 24% in the bottom and top parts of the island, corresponding to a lattice mismatch of 0.8 and 1.0% with respect to Si, respectively. Figure 1(a) shows a scheme of

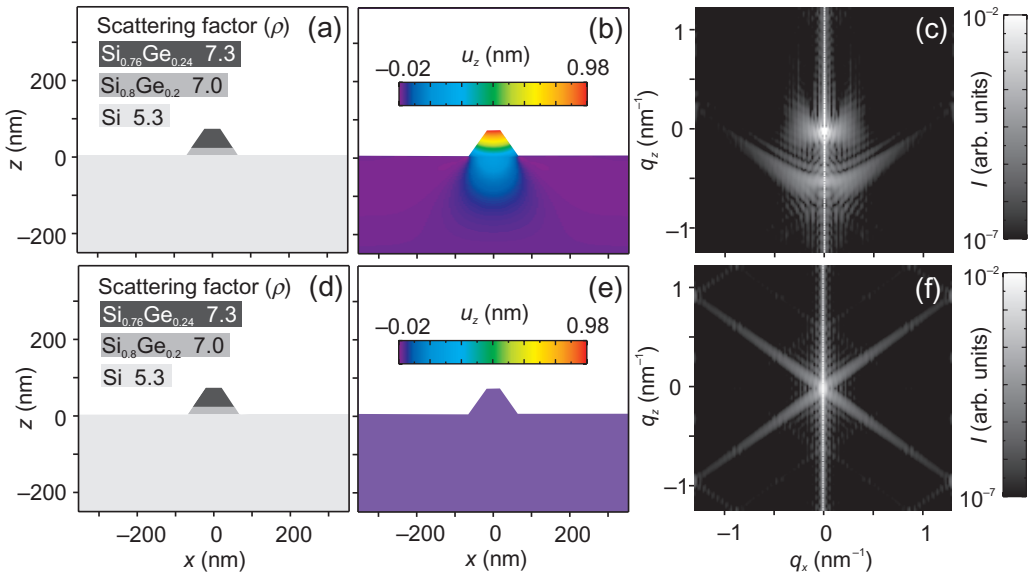

Figure 2. Comparison between the scattered intensity by a strained and an unstrained SiGe island. (a) Scattering factor corresponding to the Ge content assumed in the island, (b) finite-element calculation of the atomic displacement field u_z from the Ge content shown in (a) and (c) 2D cut off the 3D intensity distribution around the Si (004) reflection. From (d) to (f), same graphs corresponding to a SiGe island within which the u_z distribution is set to zero.

such a sample, with its crystallographic directions highlighted. In figure 2(a), a 2D cut off the SiGe islands in the xz-plane is shown, indicating the regions with different Ge concentration.

To calculate the x-ray scattered intensity, we need to know the displacement field of the atoms in the island and in the strained part of the substrate underneath. For this purpose, we perform FEM calculations using the COMSOL MULTIPHYSICS commercial FEM suite. The expansion of the SiGe domains is calculated taking into account the elastic anisotropy as well as the difference in elastic properties between Si and SiGe. For the latter, we use a linear interpolation between the values of pure Si and Ge. The boundary conditions are as follows: (i) the island and the substrate have to remain coherent at the interface, (ii) on the side faces of the substrate block only movements within the faces are allowed and (iii) the bottom face of the substrate is completely fixed. The top face of the substrate and the island are not constrained. These boundary conditions are valid if the substrate block is large enough so that at its outer faces the strain is virtually zero, which we checked by enlarging the substrate until no significant change in the strain field was observable.

From the FEM calculations, the shifts $\mathbf{u}(\mathbf{r})$ of the nodes of the FEM model with respect to the initial case are obtained. The actual displacements of the atoms of the crystal lattice can be calculated as an interpolation to the values at the FEM nodes. In the calculation of the scattered intensity, it is not necessary to obtain the displacement field at an atomic level: the construction of a pseudo-lattice with lower resolution in the range of a few nanometers per voxel is sufficient. In this way, the shifts, and also strains, are calculated with respect to a Si reference lattice in this pseudo-lattice:

$$\boldsymbol{u}_i = \boldsymbol{R}_i - \boldsymbol{R}_i^{\mathrm{ref}},$$

with $\boldsymbol{R}_i$ being the position of atom i and $\boldsymbol{R}_i^{\mathrm{ref}}$ being the position of the same atom in the reference lattice, i.e. in the absence of strain. Figure 2(b) shows the resulting displacement field distribution in the xz plane $\boldsymbol{u}(x, z)$. Displacement values range from -0.02 nm in the substrate close to the edges of the island, where compressive strain occurs, up to 0.98 nm at the top of the island, where the SiGe lattice relaxes toward its bulk lattice constant.

Figure 1(a) shows the sketch of an x-ray scattering experiment on a single SiGe nanostructure. Assuming a planar wavefield illumination, the scattered intensity around a Bragg reflection can be approximated by [30]

$$I(\boldsymbol{q}) = |\mathrm{FT}(g(\boldsymbol{r}))|^2 \tag{1}$$

with $g(\boldsymbol{r})$ being a complex-valued object

$$g(\boldsymbol{r}) = \rho(\boldsymbol{r})\mathrm{e}^{\mathrm{i}\boldsymbol{G}\cdot\boldsymbol{u}(\boldsymbol{r})},$$

where $\boldsymbol{G}$ is the chosen Bragg vector and $\rho(\boldsymbol{r})$ is the 3D scattering factor distribution within the island, which depends on the SiGe content. In the proximity of the Si (004) Bragg reflection, the phase $\phi(\boldsymbol{r})$ of the object reduces to

$$\phi(\boldsymbol{r}) = \boldsymbol{G}\cdot\boldsymbol{u}(\boldsymbol{r}) = \frac{8\pi}{a}u_z(\boldsymbol{r}), \tag{2}$$

where a is the lattice constant of the reference crystal (Si in our case). Therefore, this reflection is sensitive to the atomic displacements along the z-direction only.

Figure 1(b) shows an iso-intensity surface representation of the calculated 3D intensity distribution $I(\boldsymbol{q})$ around the Si (004) Bragg reflection obtained with equation (1), in which the fast-Fourier-transform (FFT) algorithm was employed. As we will see below, the use of the FFT algorithm is crucial to reduce computing time when propagating the wavefield back and forth between the detector and sample positions. In the calculation, the displacement distribution $u_z(\boldsymbol{r})$ obtained from the FEM calculation was used. We observe that the intensity pattern has two main contributions: at higher q_z values lies the Si (004) substrate peak and, at lower q_z values, we observe the signal arising from the SiGe island, as a consequence of the vertical tensile strain present within the SiGe island. Both peaks have a fourfold symmetry in the q_xq_y plane but are visibly asymmetric along the q_z-direction as a consequence of the strain distribution. The SiGe peak presents clear streaks perpendicular to the pyramid's facets, marked with red arrows in figure 1(b). The central intensity streak along the q_z-direction arises from the substrate surface and we will refer to it as the surface streak.

In figure 2(c), a 2D cut in the q_xq_z plane of the 3D intensity distribution is shown. The origin of reciprocal space is chosen at the Si (004) substrate peak position, which appears at the exact center of the computational window after performing the FFT. This is due to the choice of Si as a reference for the displacement field. At lower q_z values, we observe the signal from the SiGe island, presenting lower intensity values and extending over a larger region in reciprocal space as compared with the Si peak. For both peaks one can observe intensity fringes arising from the finite size of the island and the displacement distribution within the substrate.

For comparison, we have performed an identical calculation of the 3D intensity distribution $I(\boldsymbol{q})$ around the Si (004) reflection in the hypothetical case that there are no displacements within the island (figures 2(d)–(f)). Despite being non-physical, this simulation nicely illustrates the effect of strain on the intensity distribution, which is centrosymmetric in the case of an unstrained object.

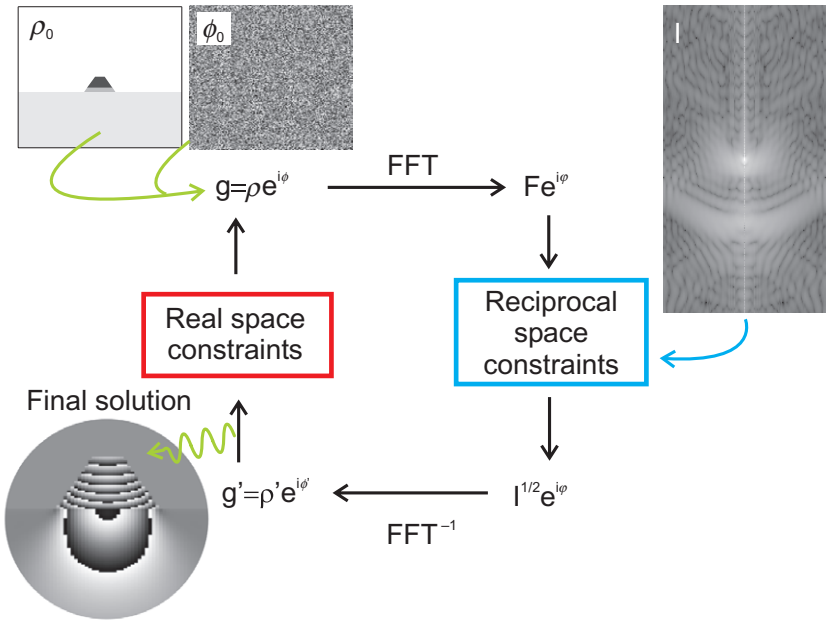

Figure 3. General scheme of the iterative phase retrieval algorithms.

3. Phase retrieval of a SiGe island on a substrate

In a coherent x-ray scattering experiment, the coherent illumination of the sample ensures that the phase of the scattered intensity carries the information on the positions of all scatterers, both on the shape of the crystal and the internal displacement field. Chemical contrast may also affect the phase relation, but this effect remains negligible if the experiment is performed far from an absorption edge of the chemical elements in the semiconductor system. Therefore, the detailed knowledge of both the amplitude and the phase of the scattered beam is highly desirable in order to retrieve the direct space description of the investigated sample. However, only the intensity, i.e. the square of the complex-valued wavefield function is experimentally accessible through photon detection. This is known as the 'phase problem'. A solution to this problem has been proposed by Sayre in 1952 [16], for reciprocal space intensity measurements performed with an oversampling higher than 2 times the Nyquist frequency of the signal. This corresponds to confining the object in direct space to a finite region called the support, which occupies half of the total volume given by the computational window. As this problem has no analytical solution, the inversion relies on numerical iterative algorithms using back and forth transforms between direct space and reciprocal space. A sketch of the algorithm is shown in figure 3. The algorithm is initiated with a direct space guess that fulfills the support condition together with a set of random phases. For measurements performed in the far-field geometry on samples small enough in order to fulfill the Born approximation conditions, the relationship between direct and reciprocal space can be described by the Fourier transform of the electron density, which is introduced as an FFT in the iterative algorithm. In order to achieve convergence of the algorithm, a set of constraints has to be applied at each iteration in direct and reciprocal space. One common direct space constraint is the support condition, which is directly related to the oversampling condition. In reciprocal space, the solution has to match the experimental

data: $F(\boldsymbol{q}) = \sqrt{I(\boldsymbol{q})}$. The convergence of the algorithm is reached when the solution fulfills both the direct and reciprocal space constraints and can be monitored by the error metric ξ^2, given by

$$\xi^2 = \frac{\sum_q \left(F(\boldsymbol{q}) - \sqrt{I(\boldsymbol{q})}\right)^2}{\sum_q I(\boldsymbol{q})}. \tag{3}$$

It can be shown that the error metric decreases at each iteration. For this reason, this algorithm is named error reduction (ER) [17], which is a variant on the original Gerchberg and Saxton algorithm [31]. However, the convergence of the ER algorithm is rather slow and it often stagnates in local minima. One common approach is to use the ER in combination with the hybrid-input–output algorithm (HIO) [17]. HIO provides an element of feedback by including the solution before applying the real space constraint $g'_n(\boldsymbol{r})$ in order to build the solution at the next iteration,

$$g_{n+1}(\boldsymbol{r}) = g_n(\boldsymbol{r}) - \beta g'_n(\boldsymbol{r}), \tag{4}$$

for regions in the object where the direct space constraints are not satisfied. The parameter β is a number ranging between 0 and 1, and is typically set to a value close to 0.9.

When convergence is reached, the error metric value given in equation (3) should converge to zero. However, for experimental data, zero error metric cannot be obtained due to noise and limited intensity dynamical range (DR). Therefore, the algorithm is interrupted after ξ^2 becomes smaller than a certain threshold. For real data, several solutions with comparable and small error metric may be found. These solutions are rejected. The search for convergence requires a lot of trial and error in order to find the correct sequence of ER and HIO, applying various direct space constraints. A solution is approved when different starting guesses (i.e. different set of initial random phases) lead to similar—almost identical—solutions for the same ER + HIO cycle combination. Small modifications of the algorithm sequence and/or the increase of the number of iterations does not affect the convergence in that case.

Applying phase retrieval algorithms to our model system of a strained SiGe island presents some specific problems. The total displacement field in the island increases with the island size and can reach values of 0.98 nm for a 140 nm island, i.e. about twice the lattice constant (see figure 2(b)), which corresponds to a phase shift of about 48 rad (16π) at the (004) Bragg reflection. This means that the real space resolution has to be small enough to sample every phase change of 2π in the object. In addition, the presence of the substrate prevents the use of a finite size support in the horizontal direction. In the vertical direction, more than half of the direct space can be set to zero, which implies that the oversampling condition is at least fulfilled in that direction. The combination of these two specificities of our system, huge phase changes and non-finite support in the horizontal direction, are the main computational difficulties that have to be solved in order to retrieve the direct space description from an intensity pattern. In order to improve the computational time, the whole numerical study is performed on a 2D sample cross section (taken in the center of the island) instead of the complete 3D data set. As the 2D cut exhibits as many phase shifts as the total 3D sample, together with the presence of the semi-infinite substrate, the mathematical problem to be solved is expected to remain the same. The determination of the inversion problem is directly related to the number of unknowns that have to be found compared with the number of known values that are given by the oversampled measurement.

It is clear from our first attempts that the inversion of the intensity pattern from the 140 nm SiGe island on a Si substrate is not accessible due to the non-finite support and the large phase changes within the sample. Indeed, we observe that the iteration process converges to the correct solution for several simpler cases: an isolated island with no substrate, an island with a truncated substrate in the horizontal direction or a weakly strained island on a substrate (for a fixed island size, the strain is artificially reduced by reducing the phase shift). The convergence is obtained using a combination of standard and modified phase retrieval algorithms. The standard algorithms are HIO and ER_{so}, where the latter is the ER with the usual support-only condition. The third algorithm, ER_{sobj}, is a modified ER with an additional constraint in real space, which imposes the knowledge of the magnitude of the complex-valued object. Finally, $ER_{so/sym}$ is the ER algorithm with the usual support constraint and with an additional axial symmetry condition for both magnitude and phase of the object. Despite those additional constraints, the intensity pattern from a 140 nm island on a substrate cannot be inverted due to the combination of large phase changes and the absence of a finite support.

Nevertheless, the case of a realistic small island on a substrate can be successfully addressed. Indeed, as the phase shift in the island is smaller for smaller island size, the inversion becomes possible for islands with base sizes below 35 nm, even with the absence of a finite support. Such SiGe islands can be fabricated and are of interest for applications [32], but are so far out of reach for CDI experiments (see section 6). Figure 4(a) shows the intensity distribution calculated from a 35 nm island, together with the result of the inversion (b). In this calculation, the direct space pixel size of the 2D sample (which is a cross section of a 3D sample) is 1.18 nm in the x-direction and 0.84 nm along the z-direction. The computational window has 150×193 pixels in horizontal and vertical directions, respectively. For perfect noiseless numerical data, where all the intensity range is preserved, we expect to obtain an error metric equal to zero, which means that the retrieved quantity matches exactly the input data. However, in some cases, we observe the retrieval of a direct space quantity that exhibits significant resemblance to the input data without, however, a perfect match. It turned out that the 35 nm island always converges in a strict way when using the following combination of phase retrieval procedure: $[200 \times ER_{sobj} + 500 \times HIO + 200 \times ER_{so/sym} + 500 \times HIO]$, several times until the error metric is below a certain error metric value necessary for a strict convergence ($\xi^2 = 10^{-9}$). A general issue is the DR that can be achieved in the experiment and the fact that the substrate signal cannot be described kinematically. In order to account for these experimental constraints, we investigated the effects of excluding the substrate peak and using a limited DR. We observe that the procedure keeps on converging strictly even after we introduce a beamstop of 5×4 pixels (horizontal $\times$ vertical) at the Si substrate Bragg peak and we limit the DR to 7 orders of magnitude (as shown on figure 4(a)). Down to a DR of 5 orders of magnitude, convergence is reached but with an error metric slightly larger than before. However, all found solutions are essentially equal to the exact solutions with very little discrepancies.

Unfortunately, the resolution and scattered intensity required to measure the 35 nm SiGe island at third-generation synchrotron sources are experimentally out of reach. Additionally, the experimental case would require to use a Si-on-insulator (SOI) wafer as a substrate due to the finite support in the vertical direction forced by the lower end of the computational window at a certain depth of the substrate. In the following, we propose other methods that allow us to retrieve the phase for larger island size and provide a more realistic approach to the substrate truncation problem.

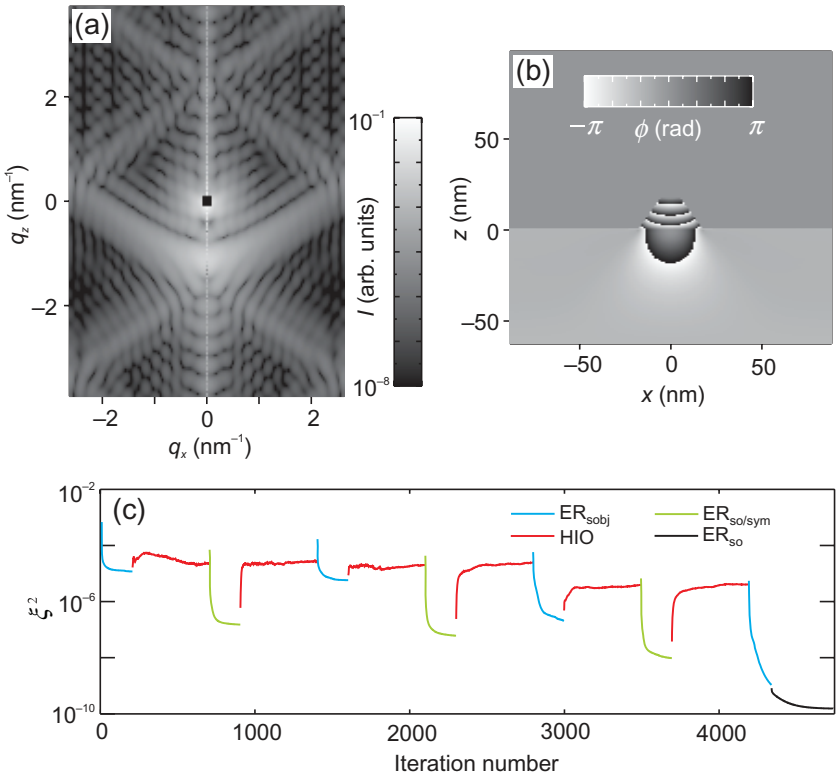

Figure 4. Example of the 2D phase retrieval of a 35 nm island on a substrate. (a) Intensity around the Si (004) reflection used as input data, calculated from a 2D cut off a 3D FEM calculation. A few pixels close to the Si (004) Bragg reflection and intensities below a DR of 7 orders of magnitude were ignored when applying the reciprocal space constraints. (b) Reconstructed phase of the object. (c) Evolution of the error metric ξ^2 as a function of the iteration number. We show in different colors the parts corresponding to the different algorithms. Details can be found in the text.

4. Phase retrieval with finite-size illumination function

A possible approach to phase retrieve the coherent diffraction pattern of an island and the surrounding substrate is directly suggested by the experimental setup used for such an experiment. Usually one focuses the x-ray beam using beryllium refractive lenses, Kirkpatrick–Baez mirrors or Fresnel zone plates, creating a well-defined x-ray wavefront both concerning its intensity as well as its phase. In order to maximize the intensity scattered by the object, the size of the focused spot should ideally match the size of the object. The most important feature of this experimental setup is the fact that the transverse section of the x-ray beam exhibits a fast decaying intensity. In this case, the complex object $g(\boldsymbol{r})$ to be retrieved is modified and is given by

$$\tilde{g}(\boldsymbol{r}) = P(\boldsymbol{r})g(\boldsymbol{r}) = P(\boldsymbol{r})\rho(\boldsymbol{r})\mathrm{e}^{\mathrm{i}\phi(\boldsymbol{r})}.$$

Here $P(\boldsymbol{r})$ is the complex-valued illumination function, which can also define the scattering region. In such a case, the phase retrieval procedure has to be modified considering the effect

of the illumination function. The input function at each iterations in the HIO algorithm must be modified to be [33]

$$\tilde{g}_{n+1}(\boldsymbol{r}) = \tilde{g}_n(\boldsymbol{r}) + [P(\boldsymbol{r})/P_{\max}(\boldsymbol{r})] \times \beta[\tilde{g}'_n(\boldsymbol{r}) - \tilde{g}_n(\boldsymbol{r})] \tag{5}$$

where $P_{\max}(\boldsymbol{r})$ is the maximum value of $P(\boldsymbol{r})$. This modification of the algorithm takes into account the fact that the intensity stems primarily from regions where the illumination function is more intense and it is expected to improve the convergence of the algorithm in two ways. First of all, the illumination function is finite, allowing the use of a finite support. Secondly, the knowledge of the illumination function is not just determining the finite extension of the object, but it is also determining an approximate value of the object's amplitude, which is dominated by the amplitude of the focused beam. The input function described in equation (5) is inspired by the ptychographic iterative engine (PIE) [34], where the illumination function is included in the complex function describing the object to retrieve. However, the PIE approach uses the redundant information of diffraction images from overlapping regions to retrieve the object. In our case, the redundancy in the information is ensured by the oversampling condition. We use only one diffraction pattern and consider that the illumination function is known.

As an example we show the phase retrieval of a 140 nm SiGe island and the substrate underneath. Figure 5(a) shows the simulated scattering pattern from an island illuminated by a focused x-ray beam. The scattering pattern is asymmetric with respect to the horizontal axis, which is an effect solely of the illumination function. As shown in figure 5(b), we have assumed a Gaussian-shaped beam with a full width at half maximum (FWHM) of 100 nm (which would represent in this case the central maximum of the Airy function created from a Fresnel zone plate setup) with a constant phase. The incident angle, which depends on the x-ray wavelength and on the probed Bragg reflection, was equal to 45°. One can observe the absence of a surface streak due to our definition of the illumination function, which uses an artificially small penetration depth. The small penetration depth is chosen in order to allow for the definition of a 3D illuminated region within the size of the computational window. In practice, however, the substrate contribution cannot be avoided using a focusing experimental setup because the depth of focus is of the order of a few hundreds of microns. Nevertheless, this contribution is anyway excluded in the analysis of experimental data because it cannot be fully described in terms of kinematical scattering. In fact, even though our approach is not completely correct, it actually describes very well the observed diffraction pattern in experiments using a focused x-ray beam of similar size to that of the nanostructure, as will be shown in section 6.

The region to be retrieved was defined by the illumination function (see figure 5(b)). Considering the DR of the scattering pattern to be 4 orders of magnitude (which is experimentally feasible), the region to be phase retrieved was considered where the illuminated region amplitude was 1×10^{-2} of the maximum amplitude. The x-ray beam was assumed to decay exponentially with a penetration depth of 0.5 μm. The complete phase map is shown in figure 5(c), where a phase variation of up to $7 \times 2\pi$ was retrieved. In essence, instead of defining the scattering region by the computational window, the scattering region was defined by the beam itself.

In figure 5(d), we show the convergence of the phase retrieval code, using a sequence of $[1500 \times \mathrm{ER}_{\mathrm{sobj}} + 50 \times \mathrm{HIO}]$, in which only the HIO algorithm was modified according to equation (5). As in the case of the previous example, the substrate and island electron densities were assumed to be known, and only the phases were retrieved. This allowed for

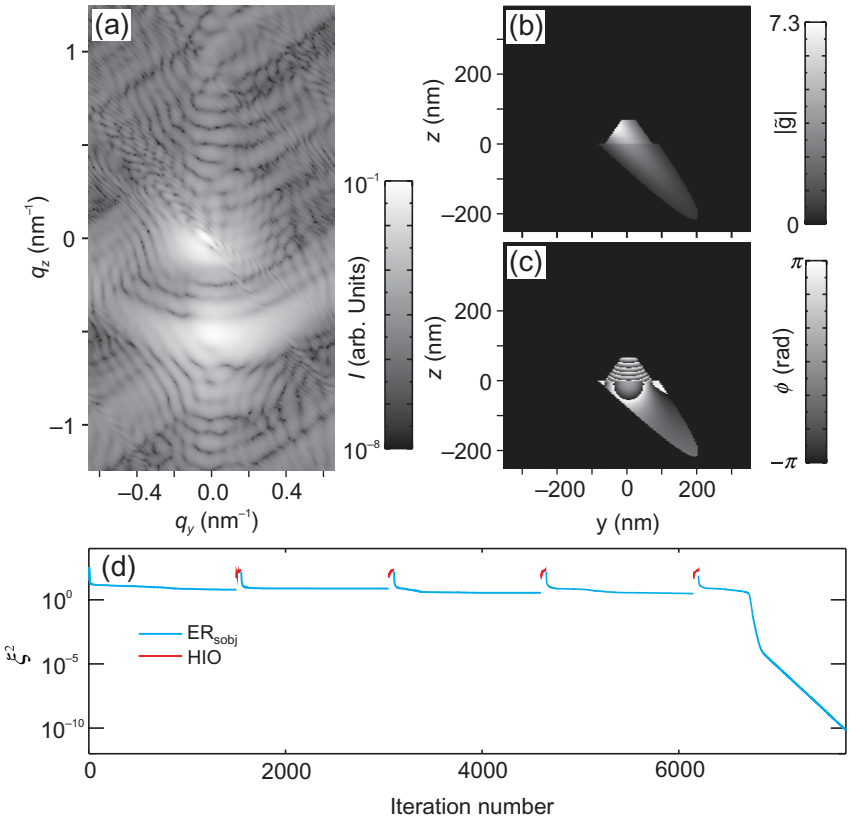

Figure 5. Example of 2D phase retrieval of a 140 nm island with a finite illumination function. (a) Intensity around the Si (004) reflection used as input data, calculated from a 2D cut of a 3D FEM calculation which has been multiplied by a 2D Gaussian distribution. (b) Reconstructed amplitude $|\tilde{g}(\boldsymbol{r})|$. (c) Reconstructed phase $\phi(\boldsymbol{r})$. (d) Evolution of the error metric ξ^2 as a function of the iteration number. We show in different colors the parts corresponding to the different algorithms. Details can be found in the text.

the convergence of all retrieval attempts. This assumption is equivalent to experiments using materials with small variations in electron density and where only strain effects are studied. It would not apply to strained nanostructures with strong variations in the electron density, in which this approach does not seem to be possible as defined above. Most importantly, this phase retrieval approach is only feasible with a well-defined and known illumination function, which can be measured using the methods described, e.g. in [35, 36].

5. Phase retrieval of an island separated from its substrate

We have shown before that the phase retrieval of an epitaxial SiGe nanostructure and its substrate is possible assuming that the structure is illuminated by a known finite-sized Gaussian function. This situation resembles a lot a real experiment in which a focused x-ray beam is used in order to illuminate a single nanostructure. However, in practice we usually only record reliable data around the SiGe peak, while the signal around the substrate Bragg peak is difficult

to measure. One needs to attenuate the beam in order not to saturate the detector, but then the noise level is increased, so that the DR is not sufficient for phase retrieval. In addition, the scattering from the unstrained substrate, as well as along the truncation rod, cannot be described correctly within kinematical scattering theory, so that the algorithms based on a simple FFT cannot be used for this part of reciprocal space. In this section we show that the signal from the SiGe peak alone corresponds, in a good approximation, to the complex density within the island alone separated from the substrate. Also, we prove that iterative phase retrieval algorithms with a finite support can be used in order to obtain the displacement field within the island alone directly from the intensity pattern around the SiGe peak only.

In a measurement of the SiGe peak around the (004) Bragg reflection in which the signal around the substrate peak is missing, it is no longer possible to use the Si lattice as a reference for the definition of the displacement fields within the island. We can use instead the lattice spacing obtained from the position in reciprocal space of maximum intensity in the SiGe peak. In figure 2(c), we observe this position at $q_{\mathrm{SiGe}}^{004} = q_{\mathrm{Si}}^{004} - 0.052\,\text{Å}^{-1}$ for a 140 nm island, corresponding to a lattice spacing of $a_{\mathrm{SiGe}} = 5.492\,\text{Å}^{-1}$. Figure 6(b) shows the phase ϕ within the island and its substrate according to equation (2) taking a_{SiGe} as reference lattice parameter in the FEM calculation of the displacement fields u_z. Because the reference lattice spacing appears in the middle of the island, we observe now small changes of the phase within the center of the island and a faster phase change at its edges and in the substrate. Figure 6(c) shows the calculated 2D intensity distribution around the SiGe (004) Bragg reflection from the complex object resulting from the amplitude distribution in figure 6(a) and the recalculated phase distribution of figure 6(b). The SiGe peak now appears centered in the window, as opposed to all previous cases where the Si lattice constant had been taken as a reference.

In order to know which information can be extracted from a measurement around the SiGe peak only, we have selected a part of the complex-valued diffracted wavefield, corresponding to the region shown in a red rectangle in figure 6(c). This region is chosen along the q_z-direction in such a way that the substrate's peak is avoided while it remains centered around the SiGe peak. The amplitude squared of the wavefield taken in this restricted reciprocal space area is shown in figure 6(d), where we have also replaced the values in the central pixel column, corresponding to the surface streak, by zeros. By means of an inverse Fourier transformation (FFT^{-1}), we obtain a complex object in direct space with an amplitude and a phase shown in figures 6(e) and (f), respectively. We note that since the complex-valued wavefield is known here, this can be done in one single step by means of an FFT^{-1} without the need of using iterative phase retrieval algorithms. Cuts across the objects in direct space with and without the substrate are compared in figures 6(g) and (h) for the scattering factor and the phase, respectively. We observe that the resolution in direct space along the vertical direction is poorer in the case of an isolated island due to the smaller range in q-space in its corresponding diffraction pattern. This simple exercise shows that the SiGe diffraction peak alone describes the original SiGe island separated from its substrate in a very good approximation, especially concerning its phase. One would not expect such a good approximation *a priori*, since the intensity corresponding to the whole system (the island and the substrate) shown in figure 6(c) contains a coherent addition of the intensities arising from the island and the substrate. The reason why it works in this particular case lies in the different lattice spacings within the island and within the substrate. Therefore, this approximation may be applied to other epitaxial systems, provided that the lattice mismatch is sufficiently large. On the other hand, the method is not yet sensitive enough to reproduce the density change in the model island at 1/3 of its height, as shown in figure 6(g).

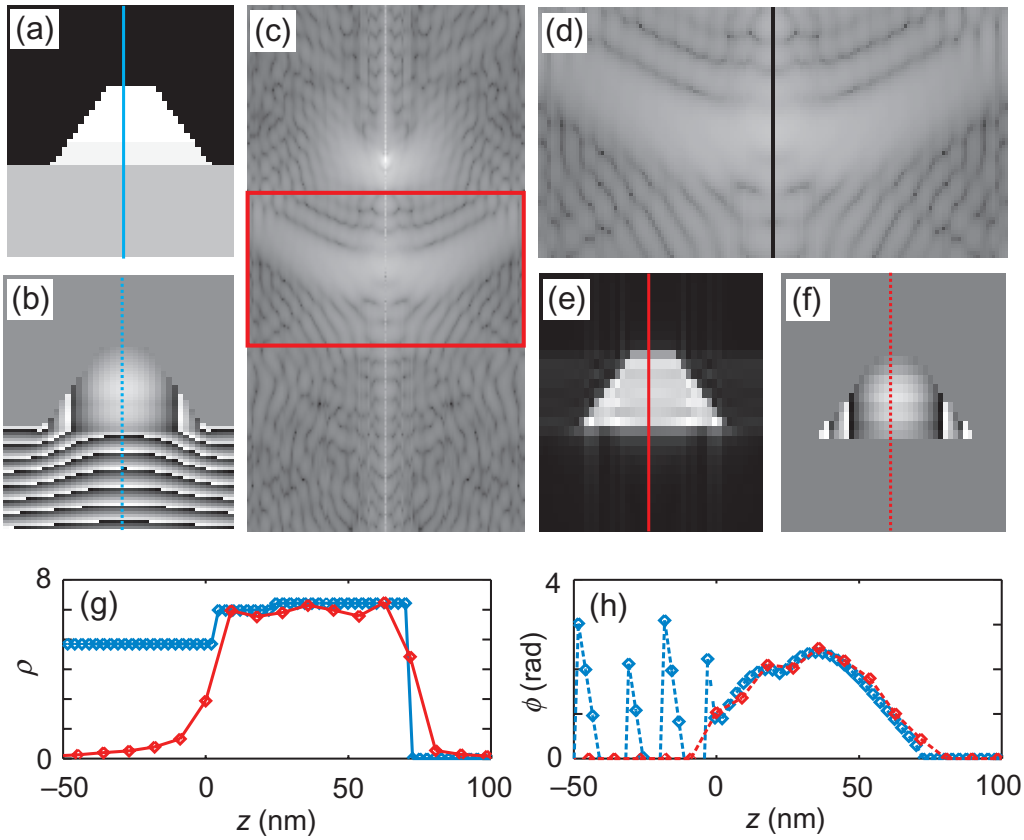

Figure 6. Illustration of the island-only approximation used for the reconstruction of the island separated from the substrate. Zoom-in of the amplitude (a) and wrapped phase (b) of a 140 nm island on a substrate in direct space when the lattice spacing from the SiGe island is used as a reference. (c) Intensity close to the (004) Bragg peak calculated from the complex object given by (a) and (b) by means of an FFT. (d) Extracted intensity from the diffraction pattern shown in (c) corresponding to the region marked within a red rectangle. Intensities in the central pixel column arising from the finite size of the substrate in the vertical direction have been set to zero. Amplitude (e) and phase (f) obtained from the complex object in reciprocal space corresponding to the region shown in (d) by means of a single inverse FFT without iterative retrieval algorithms. Vertical cuts through the amplitudes (g) and phases (h) in order to compare the obtained object with the original island on a substrate.

The next step for a model-independent analysis of the signal around the SiGe (004) peak is the demonstration of a phase retrieval directly obtained from the intensity pattern shown in figure 6(d). Such an inversion problem has two advantages with respect to the problem in section 3: (i) the object in direct space presents smaller phase variations and (ii) there is a finite support in both directions. Therefore, standard phase retrieval algorithms with a relaxed support constraint and no additional constraints can be applied in order to obtain an approximative solution for the isolated island. We performed successive series of $[500 \times \mathrm{HIO} + 200 \times \mathrm{ER}_{\mathrm{so}}]$. Initially, we assumed a support much larger than the expected size of the object, which can

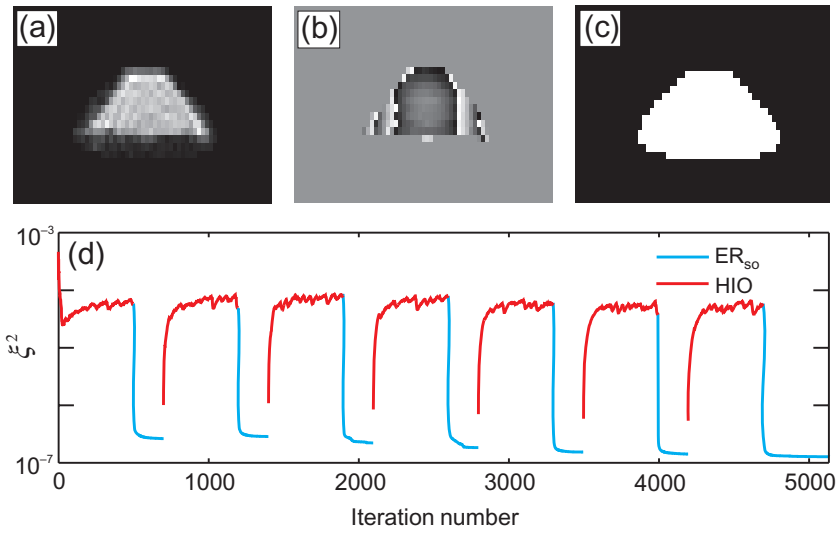

Figure 7. Reconstruction of a 140 nm island directly obtained from the intensity pattern in figure 6(d). The images show the reconstructed amplitude (a) and phase (b) in direct space, as well as the final support (c) obtained with the shrink-wrap method. In (d), we show the error metric evolution in a logarithmic scale.

be estimated from the autoconvolution function. Every 20 iterations of the HIO algorithm, a new support was created following the shrink-wrap method described in [37]. This method allowed the algorithm to progressively shrink the size of the support until a reasonable solution was found. As the criterion of convergence, we chose a minimum error metric value below which the iterative approach was interrupted. In figure 7, we show an example of phase retrieval using the region from a calculated diffraction pattern shown in figure 6(d), where the pixel values of the surface streak have been set to zero. These pixels were ignored in the algorithms when applying the constraints in reciprocal space. Figures 7(a) and (b) show the reconstructed object amplitude and phase in direct space, respectively. The results are to be compared with the expected amplitude and phase in direct space obtained from a finite region of the diffraction pattern by FFT^{-1}, shown in figures 6(e) and (f). We observe that the retrieved object resembles a lot the expected one not only in terms of shape and size, but also in density homogeneity and phase changes within the island. As we can observe in figure 7(c), the final support obtained by the shrink-wrap method has adapted very well to the shape of the object and it is only slightly larger than the reconstructed object, as expected [37]. We note that, unlike the convergence cases discussed above from a full calculated diffraction pattern (see e. g. section 3), in this case we do not expect a strict convergence due to the absence of a strict finite support in direct space for the original object: the density in figure 6(e) is not exactly equal to zero outside the object region, while in the algorithm we impose a support which is equal to zero at this region. Nevertheless, we prove here that phase changes within the island, related to the atomic displacements, can be reconstructed in a very good approximation.

We have studied the effect of a reduced DR in the diffraction pattern of figure 6(d) used for the reconstruction. The results presented above correspond to the full DR given in the calculation (7.3 orders of magnitude). In general, similar results to the ones presented above were obtained up to a DR of 5. For DRs down to 4 and 3, the reconstructed size of the island is slightly larger

than the expected one. Although the shape still resembles the original one, a slight asymmetry arises with respect to the horizontal direction in both amplitude and phase. As a consequence, phase changes are correctly retrieved in one half of the island (either the left side or the right side), but not on the corresponding opposite side. Such effects are expected in a reconstruction from experimental data, where DRs of 3 or 4 orders of magnitude can be measured, as shown in the next section. For these cases, the knowledge of the exact support, i. e. the exact shape of the island, improves the reconstructions. This could be achieved with other complementary microscopy methods, such as scanning electron microscopy.

6. Experimental state-of-the-art coherent microdiffraction

In the following, we will show an example of measured data for individual epitaxially grown SiGe islands on Si(001) of lateral base size 450 nm. As in the models shown before, the contribution of the substrate is present and partially measured; effects from a non-uniform illumination function (due to the extreme focusing) are also highlighted.

The great progress made lately in focusing x-ray optics made the achievement of sub-micron beam sizes a standard at synchrotron sources. For such experiments, it is not only the small size (in the 100 nm range) that is important, but also the relatively large photon flux in the spot and its cleanliness (no side wings, well-known illumination function, etc). Indeed, these experiments are not only photon hungry because of the small scattering volume of the probed sample (volume of the individually probed crystallite), typically below $1\mu m^3$, but also due to the spreading of the signal in the reciprocal space (size effects): the local measured intensity using an area detector will thus scale, for one pixel, with L^6, L being the lateral size of the investigated nano-object. Moreover, the direct-space resolution in CDI is determined by the total range measured in reciprocal space. Increasing the photon flux density impinging on the individual nanostructure is thus a mandatory condition for recording the data with reasonable statistics and dynamics. While in a 'classical' diffraction experiment using highly focused x-ray beams the spatial resolution is essentially given by the size of the spot used to investigate the sample, using CDI in combination with highly focused beams, a lateral resolution down to 10 nm or better can be achieved [38].

The results shown hereafter were obtained at the ID01 beamline at the European Synchrotron Radiation Facility (ESRF) in Grenoble, France. The sub-μm-sized x-ray beam was obtained using a circular (200 μm in diameter) Fresnel zone plate (FZP) with a 100 nm width outermost zone [39] and placed 129 mm upstream the sample. Working at an x-ray energy of 8 keV, an x-ray spot size of $350 \times 400\,nm^2$ (vertical$\times$ horizontal, FWHM) was obtained at the sample position. When illuminating the FZP using an aperture matching the transverse coherence length of the x-ray beam ($80 \times 20\,\mu m^2$), an illumination of the sample with a high degree of coherence is ensured, with a measured photon flux of 1.5×10^8 ph s^{-1} in the resulting x-ray spot. This setup, schematically shown in figure 1(a), is similar to the one reported in [40]: the focused x-ray beam impinges onto the sample surface at an incident angle close to the Bragg condition characteristic for the SiGe island. If the beam fully illuminates the island, the expected scattered signal (and its distribution in the reciprocal space) coming from such pyramidal shaped islands around the (004) Bragg position is shown in figure 1(b) and it can be calculated by means of a Fourier transform of the object electron density function, as explained in detail in section 2. This is also valid when the object is illuminated by a diffraction-limited focused beam exactly at the focal plane [38, 40].

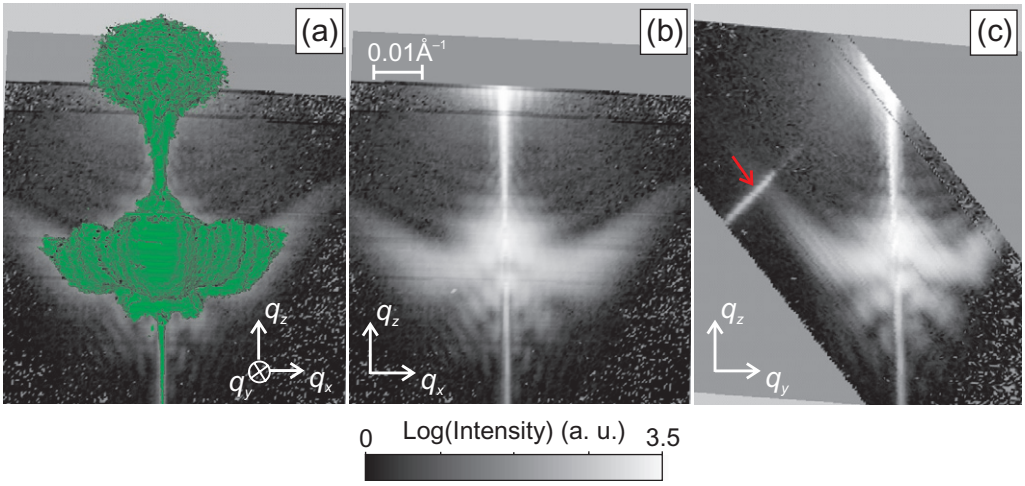

Figure 8. 3D reciprocal space map (RSM) of a single 450 nm base size SiGe island measured with an x-ray beam focused by an FZP: (a) iso-intensity surface representation together with a cut in the q_xq_z plane, (b) q_xq_z plane and (c) q_yq_z plane. The intensity streak indicated by the red arrow is an artifact of the measurement.

With the area detector (CCD) placed as shown in figure 1(a), the interception of the scattered signal with the detector is indicated by the dark plane shown in figure 1(b). In this geometry, the incident angle of the beam is scanned while recording a CCD image at each point. The resulting sequence can be reconstructed in a regular grid of the 3D reciprocal space as shown in figure 8. The 3D RSM reconstruction shown here consists of 100 images taken with a Princeton CCD camera with 55 μm pixel size placed at 0.9 m downstream the sample and spanned over 0.5° incident angle around the expected Bragg value for the island ($2\theta_{\mathrm{SiGe}} = 69.55°$). Typical exposure times were of 20 to 120 s image^{-1} and eventually the acquisition of several frames was needed, depending on the statistics. All images were corrected for incident beam intensity I_0 recorded by a beam monitor in front of the sample, dark image subtraction and flat field of the CCD.

Figure 8(a) shows a 3D view of an iso-intensity surface of the scattered signal from a single pyramid island close to the (004) Bragg reflection characteristic of the SiGe island. In this view, the rather low-intensity signal and hence prominent background (noise in the signal) prevents from seeing a lot of details, but already the main features shown in the simulated image (see figure 1(b)) can be easily identified. Many more details can be seen in the 2D cuts of the RSM along high symmetry planes (110) (q_xq_z plane in figure 8(b) and q_yq_z plane in figure 8(c)). The agreement with the simulated images (see e. g. figure 2(c)) is rather good, since all the major features (111 facets streaks, interference maxima and minima, surface streak, etc) can be identified. In fact, the measured surface streak is the substrate's crystal truncation rod. A closer lookup at the cut along the scattering plane (figure 8(c)) shows a slight asymmetry in the signal, as simulated in previous calculations when assuming a Gaussian illumination of the island with the size of the focused beam matching the size of the island (see figure 5(a)). Such an effect does not appear if a beam larger than the object size is used, as in the case of 3 μm base size pyramids exposed in [13], for which symmetric RSMs were measured for an x-ray spot size about twice as large as the object size.

In figures 8(b) and (c), fringes arising from the finite size of the island are clearly visible, indicating that the oversampling condition is fulfilled. However, attempts to phase retrieve the data from the SiGe peak have not been successful so far. Apart from the noise in the data, failure is also partly due to the low q-range measured along the x- and y-directions, $\Delta q_{x,y} \simeq 0.07\,\text{Å}^{-1}$. This corresponds to a real space resolution of about 10 nm, which is hardly sampling the 2π phase changes expected at the lower corners of an island of this size (2π phase variations every 25 nm). The measured q-range is limited by both photon flux and beam and sample stability, since a wider angular range would have to be scanned in order to perform the measurement. In fact, the enormous phase variations present in this island makes convergence impossible even with calculated data having the appropriate reciprocal space range and full DR (∼7 orders of magnitude) when using the algorithm scheme presented in section 5.

The conditions mentioned above (spot size, photon flux, materials and area detector CCD) represent almost the extreme case of measuring (in reasonable times, in this case 2–5 h) the full 3D RSM signal with a coherent beam. Attempts to record similar data for smaller objects (150 nm base size, i. e. volumes about 30 times smaller) show that the feasibility of such measurements is limited by the time required for a full measurement (several days), which is hardly compatible with beam stability requirements. However, better stability conditions and the possibility to increase the coherent photon flux in a smaller spot size would enable the measurement of smaller SiGe nanostructures, for which calculated data have been proven to converge.

7. Conclusions and outlook

We have studied the feasibility of applying CDI to highly strained epitaxial nanostructures, using SiGe islands grown on an Si (001) substrate as a model system. The final aim is to retrieve the 3D atomic displacement field distribution within an island directly from its coherent diffraction patterns measured around several Bragg reflections by means of iterative phase retrieval algorithms. For this purpose, we have systematically studied the convergence of phase retrieval algorithms using calculated data from FEM calculations. In order to speed up the convergence, we have reduced the problem to two dimensions.

We have encountered major difficulties in the convergence of standard phase retrieval algorithms caused by large phase variations ($\gg 2\pi$) within the object even for strains of the order of 0.01 and the absence of a finite support in the substrate. We have found two possible solutions that overcome the problem of a non-finite support: (i) using the knowledge of a finite illumination of the sample, which resembles the experimental case in which a focused beam is used and (ii) taking the intensity contribution from the island only, which can be inverted to provide a good approximation of the displacement field within the island separated from the substrate. The last case also overcomes the experimental problem of measuring an intensity distribution very close to a Bragg reflection of the substrate. However, the methods described here still fail in the cases of islands with base size larger than 140 nm.

On the other hand, a coherent micro-diffraction experiment has been presented on the very same SiGe epitaxial system. We have proven the possibility of recording the 3D coherent intensity distribution around the Si (004) Bragg reflection from an individual island of 450 nm base size. This measurement has been possible by the efficient focusing of the available coherent flux of a third-generation x-ray source into a spot matching the size of the island. In order to obtain similar experimental data from 140 nm islands, the beam focus should match this size and

still better stability conditions have to be fulfilled for longer exposure times. With the upgrades of third-generation synchrotron sources and the free electron lasers being installed in the near future, the required brilliance might be reached, enabling CDI experiments on single strained epitaxial nanostructures.

Acknowledgments

We thank staff at ID01 beamline at the ESRF for technical support and Martin Schmidbauer for providing the SiGe samples. Pierre Thibault and Franz Pfeiffer are gratefully acknowledged for fruitful discussions. This work was partially funded by FWF, Vienna (SFB025 IR-On) and by the French National Research agency (ANR-08-JCJC-0095-01).

References

[1] Bimberg D, Grundmann M and Ledenstov N N 1998 *Quantum Dot Heterostructures* (New York: Wiley)
[2] Ieong M, Doris B, Kedzierski J, Rim K and Yang M 2004 Silicon device scaling to the sub-10-nm regime *Science* **306** 2057–60
[3] Rahmani M D and Masri P 1993 Electronic properties of strained heterostructures *J. Physique* III **3** 1809–18
[4] Roberts M M, Klein L J, Savage D E, Slinker K A, Friesen M, Celler G, Eriksson M A and Lagally M G 2006 Elastically relaxed free-standing strained-silicon nanomembranes *Nat. Mater.* **5** 388–93
[5] Robinson R D, Sadtler B, Demchenko D O, Erdonmez C K, Wang L W and Alivisatos A P 2007 Spontaneous superlattice formation in nanorods through partial cation exchange *Science* **317** 355–8
[6] Medeiros-Ribeiro G, Bratkovski A M, Kamins T I, Ohlberg D A A and Williams R S 1998 Shape transition of germanium nanocrystals on a Si (001) surface from pyramids to domes *Science* **279** 353–5
[7] Shchukin V A, Ledentsov N N and Bimberg D 2004 *Epitaxy of Nanostructures* (Berlin: Springer)
[8] Urban K W 2008 Studying atomic structures by aberration-corrected transmission electron microscopy *Science* **321** 506–10
[9] Lamberti C 2004 The use of synchrotron radiation techniques in the characterization of strained semiconductor heterostructures and thin films *Surf. Sci. Rep.* **53** 1–197
[10] Stangl J, Holý V and Bauer G 2004 Structural properties of self-organized semiconductor nanostructures *Rev. Mod. Phys.* **76** 725–83
[11] Schülli T U, Stangl J, Zhong Z, Lechner R T, Sztucki M, Metzger T H and Bauer G 2003 Direct determination of strain and composition profiles in SiGe islands by anomalous x-ray diffraction at high momentum transfer *Phys. Rev. Lett.* **90** 066105
[12] Malachias A, Kycia S, Medeiros-Ribeiro G, Magalhães-Paniago R, Kamins T I and Williams R S 2003 3D composition of epitaxial nanostructures by anomalous x-ray diffraction: observation of a Si-rich core in Ge domes on Si(001) *Phys. Rev. Lett.* **91** 176101
[13] Mocuta C, Stangl J, Mundboth K, Metzger T H, Bauer G, Vartanyants I A, Schmidbauer M and Boeck T 2008 Beyond the ensemble average: x-ray microdiffraction analysis of single SiGe islands *Phys. Rev.* B **77** 245425
[14] Hrauda N, Zhang J J, Stangl J, Rehman-Khan A, Bauer G, Stoffel M, Schmidt O G, Jovanovich V and Nanver L K 2009 X-ray investigation of buried SiGe islands for devices with strain-enhanced mobility *J. Vac. Sci. Technol.* B **27** 912–8
[15] Robinson I and Harder R 2009 Coherent x-ray diffraction imaging of strain at the nanoscale *Nat. Mater.* **8** 291–8
[16] Sayre D 1952 Some implications of a theorem due to Shannon *Acta Crystallogr.* **5** 843
[17] Fienup J R 1982 Phase retrieval algorithms: a comparison *Appl. Opt.* **21** 2758–69

[18] Miao J, Charalambous P, Kirz J and Sayre D 1999 Extending the methodology of x-ray crystallography to allow imaging of micrometer-sized non-crystalline specimens *Nature* **400** 342–4
[19] Miao J, Ishikawa T, Johnson B, Anderson E H, Lai B and Hodgson K O 2002 High resolution 3D x-ray diffraction microscopy *Phys. Rev. Lett.* **89** 088303
[20] Robinson I K, Vartanyants I A, Williams G J, Pfeifer M A and Pitney J A 2001 Reconstruction of the shapes of gold nanocrystals using coherent x-ray diffraction *Phys. Rev. Lett.* **87** 195505
[21] Williams G J, Pfeifer M A, Vartanyants I A and Robinson I K 2003 Three-dimensional imaging of microstructure in Au nanocrystals *Phys. Rev. Lett.* **90** 175501
[22] Pfeifer M A, Williams G J, Vartanyants I A, Harder R and Robinson I K 2006 Three-dimensional mapping of a deformation field inside a nanocrystal *Nature* **442** 63–6
[23] Barty A *et al* 2008 Three-dimensional coherent x-ray diffraction imaging of a ceramic nanofoam: determination of structural deformation mechanisms *Phys. Rev. Lett.* **101** 055501
[24] Nishino Y, Takahashi Y, Imamoto N, Ishikawa T and Maeshima K 2009 Three-dimensional visualization of a human chromosome using coherent x-ray diffraction *Phys. Rev. Lett.* **102** 018101
[25] Chamard V, Diaz A, Stangl J and Labat S 2009 Structural inverstigation of InAs nanowires with coherent x-rays *J. Strain Anal. Eng. Des.* **44** 533–42
[26] Chamard V, Dollé M, Baldinozzi G, Livet F, de Boissieu M, Labat S, Picca F, Mocuta C, Donnadieu P and Metzger T H 2009 Strain analysis by inversion of coherent Bragg x-ray diffraction intensity: the illumination problem page, submitted
[27] Minkevich A A, Gailhanou M, Micha J-S, Charlet B, Chamard V and Thomas O 2007 Inversion of the diffraction pattern from an inhomogeneously strained crystal using an iterative algoritm *Phys. Rev.* B **76** 104106
[28] Schmidbauer M 2004 *X-Ray Diffuse Scattering from Self-Organized Mesoscopic Semiconductor Structures* (*Springer Tracts in Modern Physics* vol 199) (Berlin: Springer)
[29] Wiebach T, Schmidbauer M, Hanke M, Raidt H, Kohler R and Wawra H 2000 Strain and composition in SiGe nanoscale islands studied by x-ray scattering *Phys. Rev.* B **61** 5571–8
[30] Takagi S 1969 A dynamical theory of diffraction for a distorted crystal *J. Phys. Soc. Japan* **26** 1239–53
[31] Gerchberg R W and Saxton W O 1972 A practical algorithm for the determination of phase from image and diffraction plane pictures *Optik* **35** 235–46
[32] Dais C, Mussler G, Sigg H, Müller E, Solak H H and Grutzmacher D 2009 Evolution and stability of ordered SiGe islands grown on patterned Si(100) substrates *J. Appl. Phys.* **105** 122405
[33] Rodenburg J M and Faulkner H M L 2004 A phase retrieval algorithm for shifting illumination *Appl. Phys. Lett.* **85** 4795–7
[34] Faulkner H M L and Rodenburg J M 2005 Error tolerance of an iterative phase retrieval algorithm for moveable illumination microscopy *Ultramicroscopy* **103** 153–64
[35] Quiney H M, Peele A G, Cai Z, Paterson D and Nugent K A 2006 Diffractive imaging of highly focused x-ray fields *Nat. Phys.* **2** 101–4
[36] Thibault P, Dierolf M, Menzel A, Bunk O, David C and Pfeiffer F 2008 High-resolution scanning x-ray diffraction microscopy *Science* **321** 379–82
[37] Marchesini S, He H, Chapman H N, Hau-Riegge S P, Noy A, Howells M R, Weierstall U and Spence J C H 2003 X-ray image reconstruction from a diffraction pattern alone *Phys. Rev.* B **68** 140101
[38] Schroer C G, Boye P, Feldkamp J M, Patommel J, Schropp A, Schwab A, Stephan S, Burghammer M, Schöder S and Riekel C 2008 Coherent x-ray diffraction imaging with nanofocused illumination *Phys. Rev. Lett.* **101** 090801
[39] Jefimovs K, Bunk O, Pfeiffer F, Grolimund D, van der Veen J F and David C 2007 Fabrication of Fresnel zone plates for hard x-rays *Microelectron. Eng.* **84** 1467–70
[40] Diaz A, Mocuta C, Stangl J, Mandl B, David C, Vila-Comamala J, Chamard V, Metzger T H and Bauer G 2009 Coherent diffraction imaging of a single epitaxial InAs nanowire using a focused x-ray beam *Phys. Rev.* B **79** 125324